Effects of doping on an unusual smectic-C^*_α–smectic-C^*_{FI2}–smectic-C^* phase sequence

B. K. McCoy,[1,2] Z. Q. Liu,[1,3] S. T. Wang,[4] Lidong Pan,[1] Shun Wang,[1] H. T. Nguyen,[5] R. Pindak,[4] and C. C. Huang[1]
[1]*School of Physics and Astronomy, University of Minnesota, Minneapolis, Minnesota 55455, USA*
[2]*Department of Mathematics and Physics, Azusa Pacific University, Azusa, California 91702, USA*
[3]*Department of Physics, Astronomy and Engineering Science, St. Cloud State University, St. Cloud, Minnesota 56301, USA*
[4]*NSLS, Brookhaven National Laboratory, Upton, New York 11973, USA*
[5]*Centre de Recherche Paul Pascal, CNRS, Université Bordeaux I, Avenue A. Schweitzer, F-33600 Pessac, France*
(Received 29 January 2008; published 6 June 2008)

The compound 10OHF has a partially inverted phase sequence, unique among the series of *n*OHF homologous compounds and all other known liquid crystals, with the smectic-C^*_{FI2} (SmC^*_{FI2}) phase occurring at higher temperature than the smectic-C^* (SmC^*) phase. We present ellipsometric data to identify the phase sequences of 9OHF, 10OHF, 11OHF, and 12OHF. Binary mixtures of 10OHF with C11, a compound with the typical phase sequence among the smectic phases, show that the unusual phase sequence of 10OHF stabilizes upon mixing and that SmC^*_{FI2} predominates over SmC^* throughout the entire mixing phase diagram. In thin films of some mixtures, surface interactions induce a reentrant SmC^*_{FI2}-SmC^*-SmC^*_{FI2} transition in the rest of the film.

DOI: 10.1103/PhysRevE.77.061704 PACS number(s): 64.70.M−, 77.84.Nh

I. INTRODUCTION

The tilted chiral smectic variant phases are of interest because several similar phases exist, each with distinct polarization and optical properties. Over the last several years, the interlayer orientational structures of the various tilted chiral smectic phases have been well established by optical experiments and resonant x-ray diffraction. However, the underlying causes for the phases are not well understood. The molecules have an elongated rodlike shape. In addition to the layered structure, the molecular axes are oriented along a preferred direction. In the smectic phases, the molecules are arranged in molecular monolayers with a liquidlike in-plane arrangement of the positions of the molecules. When the preferred direction is parallel to the layer normal, the phase is denoted as smectic-*A* (Sm*A*). The molecules may also be tilted away from the layer normal, with the vector $\vec{c}$ describing the direction of the tilt. The magnitude of $\vec{c}$ is proportional to the sine of the angle between the molecular axis and the layer normal. The tilt angle is uniform in all layers throughout the bulk sample. $\vec{c}$ is uniform within each layer; however, the direction of $\vec{c}$ may be different in different layers. The tilted chiral smectic variant phases are distinguished by the arrangements of the $\vec{c}$ vectors from layer to layer. In the smectic-C^* (SmC^*) phase, the $\vec{c}$ vectors in all of the layers constitute a helical structure, imposed by molecular chirality. The pitch of the helix in SmC^* is on the order of a few hundred smectic layers, so the $\vec{c}$ vectors are nearly parallel in any two adjacent layers. The smectic-C^*_α (SmC^*_α) phase has a layer-to-layer arrangement of the $\vec{c}$ vectors with the same helical symmetry, though the pitch is much shorter, on the order of ten layers. The smectic-C^*_{FI2} (SmC^*_{FI2}) and smectic-C^*_{FI1} (SmC^*_{FI1}) have commensurate arrangements of $\vec{c}$ with four and three layer unit cells, respectively. The orientations of $\vec{c}$ within the unit cells are described by the distorted clock model [1]. The smectic-C^*_A (SmC^*_A) phase has antiparallel $\vec{c}$ in adjacent layers. A helical structure with long pitch is superimposed on these short-range structures in SmC^*_{FI2}, SmC^*_{FI1}, and SmC^*_A.

Because the molecules are chiral, mirror symmetry is broken when the molecular axis is tilted away from the layer normal and a polarization is allowed [2]. The polarization of each layer is within the layer plane and perpendicular to $\vec{c}$. The magnitude of the polarization is approximately proportional to the tilt angle. The net polarization of a sample is perpendicular to the sum of $\vec{c}$ for all layers. Because the arrangements of $\vec{c}$ differ for each of the tilted chiral variant phases, the phases have different polarization properties. Both SmC^* and SmC^*_α are best described as helielectric, though SmC^* is often identified as ferroelectric if the number of layers in the sample is less than the helical pitch. SmC^*_{FI1} is ferrielectric, with a smaller net polarization than SmC^*. SmC^*_{FI2} and SmC^*_A are antiferroelectric, though the net polarization may be nonzero due to surface layers and the superimposed long pitch.

Out of several hundred chiral compounds that have been studied previously, almost all compounds showed the typical phase sequence Sm*A*-SmC^*_α-SmC^*-SmC^*_{FI2}-SmC^*_{FI1}-SmC^*_A; some of these phases may be missing in most compounds. A brief description of experimental methods is given in Sec. II. In Sec. III, we present phase sequences for four homologous compounds: 9OHF, 10OHF, 11OHF, and 12OHF. The molecular structures and relevant phase transition temperatures are given in Fig. 1. 10OHF has an unusual phase sequence, with SmC^* and SmC^*_{FI2} inverted from their order in the typical phase sequence. In Sec. IV, we briefly review and expand a previous result [3] that, upon doping, the SmC^*_{FI2} phase in the unusual phase sequence of 10OHF is surprisingly stabilized. In binary mixtures of 10OHF with C11 (Sec. V), a compound with the typical phase sequence, SmC^* disappears in favor of SmC^*_{FI2} on both the 10OHF-rich and C11-rich sides of the phase diagram, in confirmation of Refs. [3,4]. In two mixtures of 10OHF with C11, an unusual transition was observed in thin films. In Sec. VI, we show that this unusual transition is a reentrant SmC^*_{FI2}-SmC^*-SmC^*_{FI2} transition induced by interactions between the surfaces of a thin freestanding film.

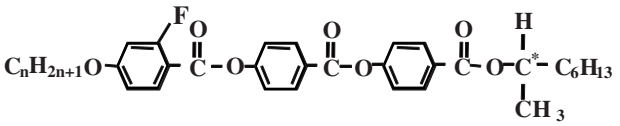

9OHF: SmA (63 °C) SmC*$_\alpha$ (52 °C) SmC*

10OHF: SmA (86 °C) SmC*$_\alpha$ (76 °C) SmC*$_{FI2}$ (69 °C) SmC*

11OHF: SmA (94 °C) SmC*$_\alpha$ (89 °C) SmC*

12OHF: SmA (102 °C) SmC*$_\alpha$ (98 °C) SmC*

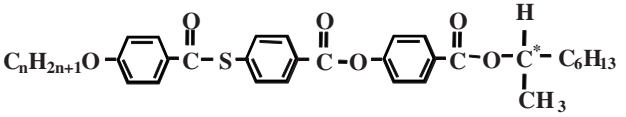

C9: SmA (115 °C) SmC*$_\alpha$ (109 °C) SmC*$_{FI2}$ (85 °C) SmC*$_A$

C11: SmA (124 °C) SmC*$_\alpha$ (122 °C) SmC* (100 °C) SmC*$_{FI2}$

FIG. 1. Chemical structures and phase sequences for the homologous series *n*OHF (top) and C*n* (bottom). The numbers in each compound name correspond to the number of carbons in the alkyl chain at the left end of the molecule. The phase sequences upon cooling for the compounds which are relevant to this work are also given.

II. EXPERIMENTAL METHODS

Null transmission ellipsometry (NTE) uses differential transmittivity for incident light polarized along two orthogonal directions to probe sample structure [5]. When light passes through the sample, the elliptical polarization state changes by an amount dependent on the thickness of the film and the optical tensor. An elliptically polarized beam is produced by a polarizer and a quarter-wave plate. To achieve a null transmission state of the ellipsometer, the ellipticity of the incident polarization is adjusted, by changing the angle between the axes of the polarizer and the quarter-wave plate, until the transmitted beam is linearly polarized. Another polarizer acting as an analyzer crosses the polarization of the transmitted light to produce a null signal. Two ellipsometric parameters Ψ and Δ define the null transmission state. Ψ is the orientation of the analyzer axis. Δ is the phase lag between the $\hat{p}$ and $\hat{s}$ components of the incident light necessary to produce the linearly polarized transmitted light; with the orientation of the quarter-wave plate fixed, Δ is related to the orientation of the upstream polarizer.

The sample is a free-standing film stretched across a circular hole in a glass film plate, housed inside a two-stage oven. 633 nm laser light is transmitted through the film at a 45° angle with respect to the film normal. Eight electrodes symmetrically spaced around the hole apply an electric field in the plane of the film. The electric field can be set to any direction within the film plane. The angle between the electric field and the projection of the incident wave vector on the film plane is defined as α. The net polarization of the film aligns with the electric field. Since Δ is related to the optical biaxiality of the sample, optically biaxial samples produce a strong dependence of Δ on α. If the electric field is rotated, the molecules rotate about the layer normal. The tilted smectic variant phases each have a characteristic rotational symmetry, so the phases can be identified by rotating the electric field.

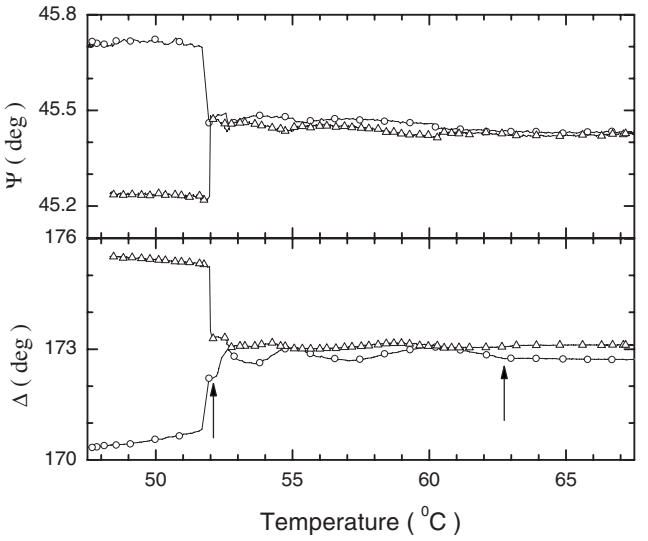

FIG. 2. Ψ and Δ vs temperature for a 58-layer film of 9OHF. The electric field orientation was held constant at α=90° (circles) or 270° (triangles) during each cooling ramp. The cooling rate was 150 mK/min for α=90° and 50 mK/min for α=270°. Arrows mark the transition temperatures. Symbols are shown only for every tenth data point during each ramp for clarity.

Resonant x-ray diffraction (RXRD) [1,6] identifies the symmetry of the smectic phases more directly. By measuring the momentum transfer of x rays along the layer normal, Q_z, the spatial periodicity of the smectic phase is obtained. In this case, the momentum space location of the Bragg peaks gives the spacing of the smectic layers. The C*n* compounds contain one sulfur atom per molecule. With the x-ray energy tuned to the $K\alpha$ absorption edge of sulfur, the x-ray scattering structure factor becomes a tensor sensitive to the orientation of the sulfur bonds [7]. The tilted smectic variant phases have orientational periodicity in addition to the layered structure. Resonant diffraction peaks measure the orientational periodicity. The difference in the reciprocal space locations of the resonant peaks and the associated Bragg peaks gives the size of the unit cell for ordering of the tilt orientations.

III. PHASE SEQUENCES OF THE *n*OHF HOMOLOGOUS COMPOUNDS

Laux *et al.* [8] have performed preliminary measurements on an interesting series of homologous compounds, *n*OHF, to identify the phase sequences for each member of the series. The homologous compounds differ by the number of methyl groups in the end chain. Laux *et al.* were not able to unambiguously determine the identity of all of the phases. Using the complementary methods of null transmission ellipsometry and resonant x-ray diffraction, we can remove any ambiguity and classify each phase.

We have studied 9OHF using NTE (Fig. 2). The large span of Ψ and Δ at the lowest temperatures shown in the figure indicates that the film is highly biaxial and the phase is SmC^* [9]. The oscillations of Δ between 52 and 63 °C occur in the SmC^*_α phase as the helical pitch and the number of

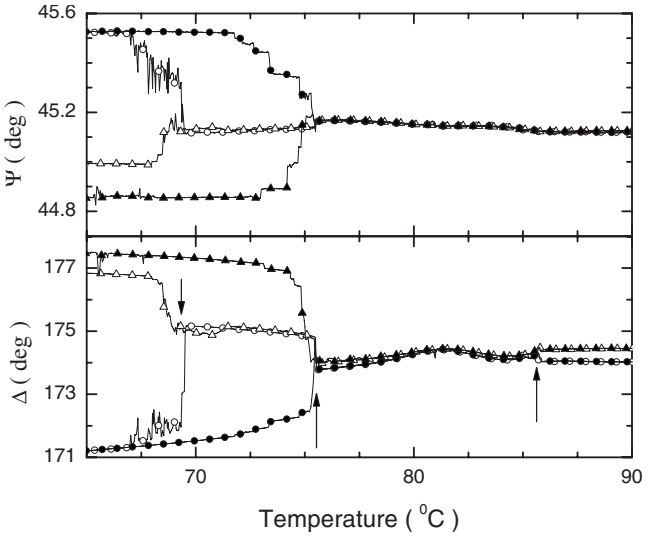

FIG. 3. Ψ and Δ vs temperature for a 60-layer film of 10OHF while ramping at 70 mK/min. The electric field orientation was held constant at $\alpha=90°$ (circles) or 270° (triangles) during each ramp. Both cooling (open symbols) and heating (filled symbols) ramps are shown. Arrows mark the transition temperatures.

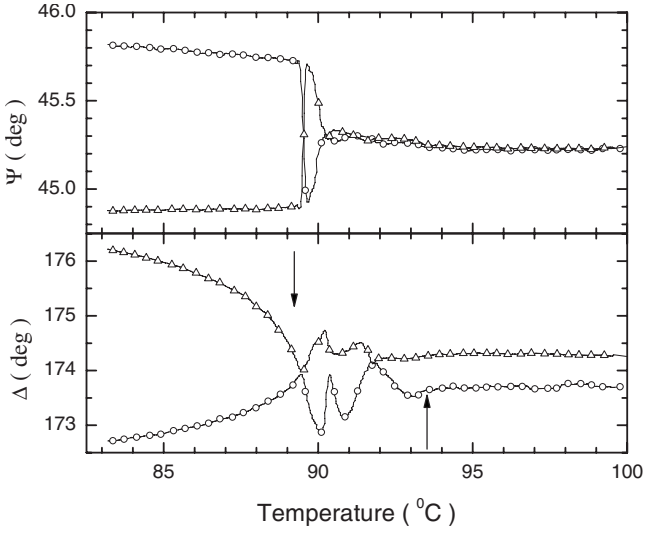

FIG. 4. Ψ and Δ vs temperature for a 58-layer film of 11OHF while cooling. Rotations of α were performed during the cooling in 0.05 °C steps. Ψ and Δ were extracted from the rotation data at $\alpha=90°$ (circles) or 270° (triangles). Arrows mark the transition temperatures.

turns of the helix within the film evolve with temperature [10]. Above 63 °C, both Ψ and Δ are nearly independent of the electric field orientation α; the phase is Sm*A*. A small biaxiality due to tilted surface layers produces a small difference between the values of Δ at $\alpha=90°$ (Δ_{90}) and 270° (Δ_{270}) [11,12]. The phase sequence for 9OHF is $\mathrm{Sm}A \overset{63\ °\mathrm{C}}{\leftrightarrow} \mathrm{Sm}C_{\alpha}^{*} \overset{52\ °\mathrm{C}}{\leftrightarrow} \mathrm{Sm}C^{*}$. The film was cooled further, but no additional smectic phases were observed before the film crystallized. Upon heating the film, the phase sequence was reproduced.

In 10OHF (Fig. 3), the phase sequence is different while cooling. Sm*A* and $\mathrm{Sm}C_{\alpha}^{*}$ remain as the two highest-temperature smectic phases. The phase is SmC^{*} before the film crystallizes. During cooling ramps, another phase appears between $\mathrm{Sm}C_{\alpha}^{*}$ and SmC^{*}. Laux *et al.* identified this phase as either $\mathrm{Sm}C_{FI2}^{*}$ or $\mathrm{Sm}C_{FI1}^{*}$. Rotations of α in this region show that Ψ and Δ both have 180° symmetry, indicating either $\mathrm{Sm}C_{FI2}^{*}$ or $\mathrm{Sm}C_{A}^{*}$. Some noise is present in the signal while the phase is $\mathrm{Sm}C_{FI2}^{*}$ due to 2π walls moving across the laser beam. RXRD experiments confirm that the phase is $\mathrm{Sm}C_{FI2}^{*}$ [3,13]. Thus, upon cooling, the phase sequence $\mathrm{Sm}A \overset{86\ °\mathrm{C}}{\leftrightarrow} \mathrm{Sm}C_{\alpha}^{*} \overset{76\ °\mathrm{C}}{\leftrightarrow} \mathrm{Sm}C_{FI2}^{*} \overset{69\ °\mathrm{C}}{\leftrightarrow} \mathrm{Sm}C^{*}$ is inverted from the sequence observed in most liquid crystals; typically SmC^{*} appears at higher temperatures than $\mathrm{Sm}C_{FI2}^{*}$. The $\mathrm{Sm}C_{FI2}^{*}$ phase did not appear while heating; a direct transition from SmC^{*} to $\mathrm{Sm}C_{\alpha}^{*}$ occurs at 76 °C, the same point as the $\mathrm{Sm}C_{\alpha}^{*}$-$\mathrm{Sm}C_{FI2}^{*}$ transition while cooling. $\mathrm{Sm}C_{FI2}^{*}$ is a monotropic phase in pure 10OHF [14].

The phase sequence for 11OHF is the same as the phase sequence for 9OHF. Figure 4 shows Ψ and Δ at two orientations of the electric field while cooling a film of 11OHF. Ψ begins to increase at 93.6 °C as the film thickness decreases when the molecules tilt below the Sm*A*-$\mathrm{Sm}C_{\alpha}^{*}$ transition. Oscillations in Ψ and Δ due to the increase in the pitch in the $\mathrm{Sm}C_{\alpha}^{*}$ phase also begin simultaneously. The oscillations cease at 89.2 °C when the helical pitch becomes greater than the film thickness. The pitch increases continuously from the short pitch in the $\mathrm{Sm}C_{\alpha}^{*}$ phase to the longer pitch in the SmC^{*} phase [15]. The $\mathrm{Sm}C_{\alpha}^{*}$-Sm$C^{*}$ transition is continuous, in contrast to 9OHF, in which some hysteresis was evident in the $\mathrm{Sm}C_{\alpha}^{*}$-Sm$C^{*}$ transition temperature, indicating a first-order $\mathrm{Sm}C_{\alpha}^{*}$-Sm$C^{*}$ transition. The ellipsometric parameters Ψ and Δ also change discontinuously at the $\mathrm{Sm}C_{\alpha}^{*}$-Sm$C^{*}$ transition in 9OHF, indicating a discontinuity in the helical pitch.

12OHF shows the same phase sequence as 9OHF and 11OHF. The oscillations in the $\mathrm{Sm}C_{\alpha}^{*}$ phase are more closely spaced than in Figs. 2 and 4, because the number of turns of the $\mathrm{Sm}C_{\alpha}^{*}$ helix changes more rapidly with temperature in the thicker film shown in Fig. 5 [16]. The data in Fig. 5 appear noisy because the cooling rate was too fast to resolve all of the oscillations of the $\mathrm{Sm}C_{\alpha}^{*}$ helix. The $\mathrm{Sm}C_{\alpha}^{*}$-Sm$C^{*}$ transition is again continuous. The phase sequence for 12OHF is $\mathrm{Sm}A \overset{102\ °\mathrm{C}}{\leftrightarrow} \mathrm{Sm}C_{\alpha}^{*} \overset{98\ °\mathrm{C}}{\leftrightarrow} \mathrm{Sm}C^{*}$. Over the entire homologous sequence of compounds, the transition temperatures increase as the length of the terminal alkyl chain increases. The unusual phase sequence on cooling in 10OHF is unique among this homologous sequence, and in fact unique among all known liquid crystals.

IV. MIXTURES OF 10OHF WITH C9

Wang *et al.* [3,13] studied binary mixtures of 10OHF with C9 in order to examine the stability of the unusual phase sequence of 10OHF. Both components of the mixtures were right-handed enantiomers of the chiral compounds, so that the mixture was optically pure [17]. The chemical

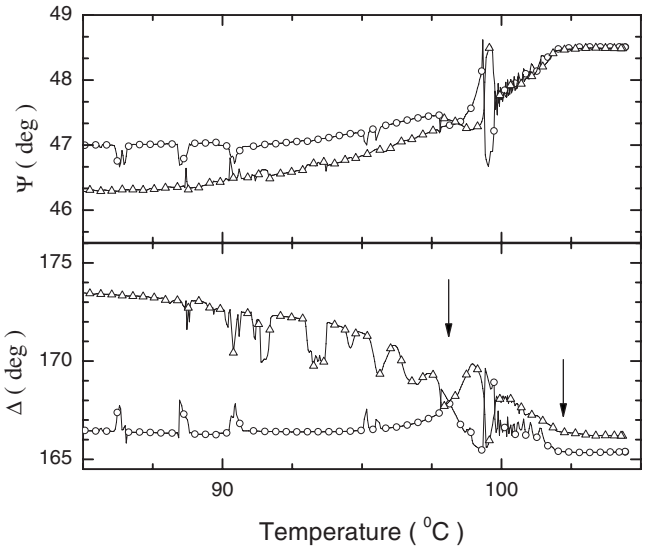

FIG. 5. Ψ and Δ vs temperature for 268-layer film of 12OHF while cooling at 70 mK/min. The electric field orientation was held constant at α=90° (circles) or 270° (triangles) during each cooling ramp. Arrows mark the transition temperatures.

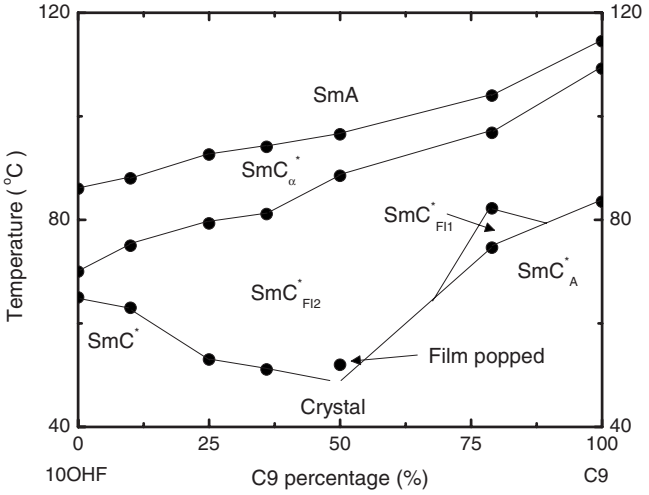

FIG. 6. Phase diagram for binary mixtures of 10OHF with C9. The circles mark the transition temperatures for each mixture studied. In the 50% mixture, the film crystallized before entering the SmC^* phase.

structure of C9 (see Fig. 1) is very similar to that of 10OHF in order to ensure miscibility of the two compounds. The sulfur atom in the core of the C9 molecules allows for RXRD studies. The phase sequence of C9 is $SmA \overset{115\ °C}{\leftrightarrow} SmC^*_\alpha \overset{109\ °C}{\leftrightarrow} SmC^*_{FI2} \overset{85\ °C}{\leftrightarrow} SmC^*_A$, similar to the phase sequence of 10OHF during cooling but lacking SmC^* below SmC^*_{FI2}. NTE studies of mixtures with 10%, 25%, 36%, 50%, and 79% C9 with 10OHF by weight (x) were conducted to find the transition temperatures and phase sequences. The mixture with 25% C9 was further studied using RXRD. Resonant peaks located at $Q_z/Q_0=5/4$ confirmed that the phase with 180° symmetry in Fig. 3 is SmC^*_{FI2} [6,18]; Q_0 denotes the momentum transfer for the (001) Bragg peak. Ψ and Δ vs α curves in this phase had the same shape as in pure 10OHF and the other mixtures as they did in the 25% C9 mixture. By extrapolation, the phase sequence of pure 10OHF while cooling is SmA-SmC^*_α-SmC^*_{FI2}-SmC^*. The identities of the other phases were similarly deduced using NTE, and then confirmed using RXRD with the 25% C9 mixture. One surprising result occurred for the 79% C9 mixture. At a temperature between the SmC^*_{FI2} and SmC^*_A phases, a resonant peak appeared at $Q_z/Q_0=4/3$, indicating a three-layer unit cell and the SmC^*_{FI1} phase. The SmC^*_{FI1} phase was also visible in the NTE data. Even though SmC^*_{FI1} did not occur in either of the pure compounds, 10OHF or C9 [19], the phase was present in the mixing phase diagram.

Figure 6 summarizes the phases present in the binary mixtures. The temperature window for the SmC^*_{FI2} phase increases and the transition temperature to SmC^* decreases as the percentage of C9 in the mixture increases for $x<50\%$. For $x>50\%$, the transition temperature from SmC^*_{FI2} to SmC^*_A also decreases while moving away from the pure compound C11. The SmC^*_{FI2} phase is stabilized by doping. Two recent theoretical advances [20,21] support this observation. Olson *et al.* have proposed a phenomenological free energy expansion including only short-range interactions, with terms coupling the $\vec{c}$ vector in each layer to nearby layers, up to the third nearest neighbor. Each of the tilted smectic phases is stable in this model over some region of the space mapped out by two parameters: the nearest-neighbor and next-nearest-neighbor layer interaction strengths. To obtain the normal phase sequence, the next-nearest-neighbor interaction strength must be nonmonotonic with temperature. However, the unusual phase sequence of 10OHF can be obtained with both interaction parameters varying monotonically with temperature. Another model by Hamaneh and Taylor uses a phenomenological short-range interaction and an entropic long-range interaction from fluctuations of the smectic layers [21,22] to predict the existence of all of the tilted smectic phases. In this model, monotonic variations of both interaction strength also can produce the unusual phase sequence of 10OHF.

V. MIXTURES OF 10OHF WITH C11

While it is somewhat surprising that the unusual phase sequence in 10OHF stabilizes upon mixing with C9, as indicated by the increasing temperature window for the SmC^*_{FI2} phase and the change of SmC^*_{FI2} from monotropic to thermotropic behavior, because pure C9 does not contain the SmC^* phase no other phase must be eliminated in order for the SmC^*_{FI2} phase to become stable. In other words, the stability region for SmC^*_{FI2} can connect smoothly across the mixing phase diagram as seen in Fig. 6. Alternatively, if 10OHF were mixed with a dopant that exhibits the SmC^* phase at higher temperature than the SmC^*_{FI2} phase as in the normal phase sequence, either SmC^* or SmC^*_{FI2} could connect smoothly across the phase diagram or another phase could interrupt both SmC^* and SmC^*_{FI2}. Such a binary mixture would provide a more stringent test of the conclusion of Ref. [3] that the unusual phase sequence stabilizes upon mixing. C11, a homolog of C9, is one suitable compound containing

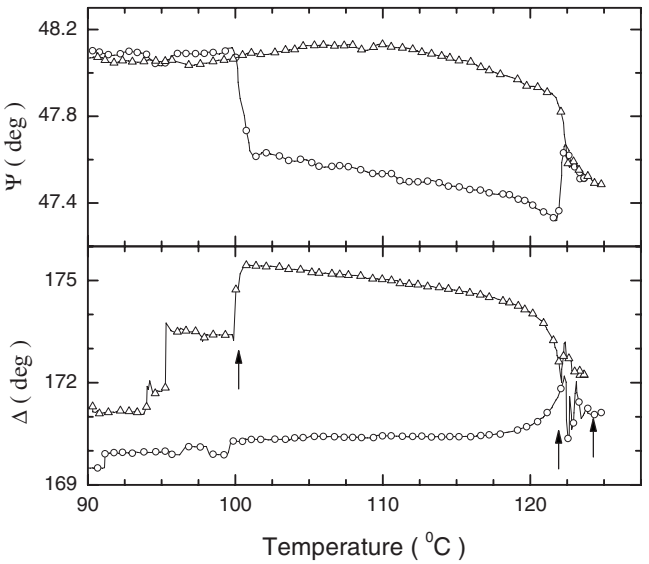

FIG. 7. Ψ and Δ vs temperature for a 47-layer film of C11 while ramping at 150 mK/min. The electric field orientation was held constant at α=90° (circles) or 270° (triangles) during each cooling ramp. Arrows mark the transition temperatures.

SmC^* in the normal phase sequence for further studies of binary mixtures with 10OHF. Ψ and Δ vs temperature from a 47-layer film of C11 are shown in Fig. 7. The phase sequence for C11 is SmA $\overset{124\ °C}{\leftrightarrow}$ SmC^*_α $\overset{122\ °C}{\leftrightarrow}$ SmC^* $\overset{100\ °C}{\leftrightarrow}$ SmC^*_{FI2}. Previous RXRD studies [23] have shown that the helical pitch has a small discontinuity at the SmC^*_α-SmC^* transition and that the phase with 180° symmetry below 100.3 °C is SmC^*_{FI2}. The steps in Δ near 100 °C are likely due to a surface transition in addition to the bulk SmC^*-SmC^*_{FI2} transition [24].

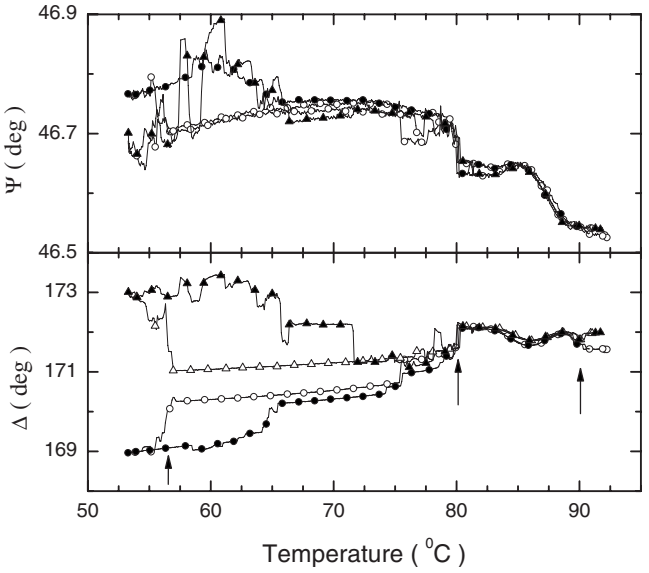

FIG. 8. Ψ and Δ vs temperature for a 51-layer film of 11% C11 with 89% 10OHF while ramping at 150 mK/min. The electric field orientation was held constant at α=90° (circles) or 270° (triangles) during each ramp. Both cooling (open symbols) and heating (filled symbols) are shown. Arrows mark the transition temperatures while cooling.

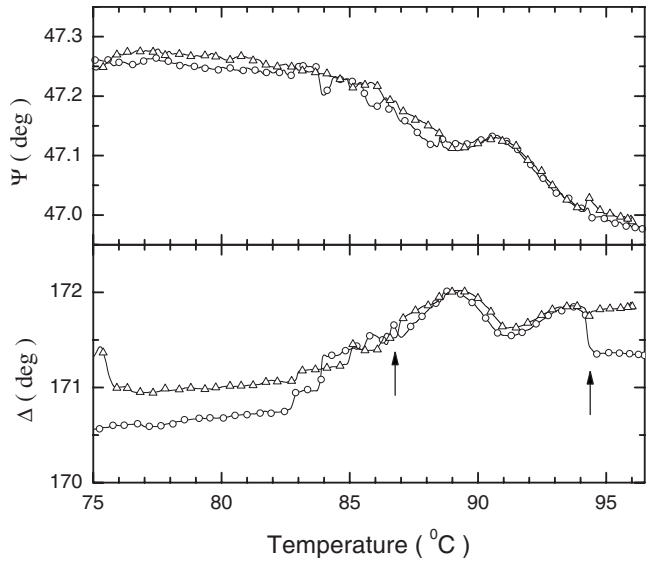

FIG. 9. Ψ and Δ vs temperature for a 49-layer film of 67% C11 with 33% 10OHF while ramping at 150 mK/min. The electric field orientation was held constant at α=90° (circles) or 270° (triangles) during each cooling ramp. Arrows mark the transition temperatures.

Using NTE and RXRD, we have studied six mixtures of 10OHF and C11: 11%, 25%, 67%, 72%, 74.4%, and 83% of C11. NTE data temperature ramps for three representative mixtures among the set of mixtures studied, 11%, 67%, and 83%, are shown in Figs. 8–10. The mixture of 11% C11 (Fig. 8) has the same phase sequence as 10OHF. SmC^*_{FI2} extends over a temperature window of about 23 K in the mixture, much greater than the temperature window of about 8 K for SmC^*_{FI2} in pure 10OHF. There is hysteresis in the SmC^*-SmC^*_{FI2} transition, but SmC^*_{FI2} is present for about 15

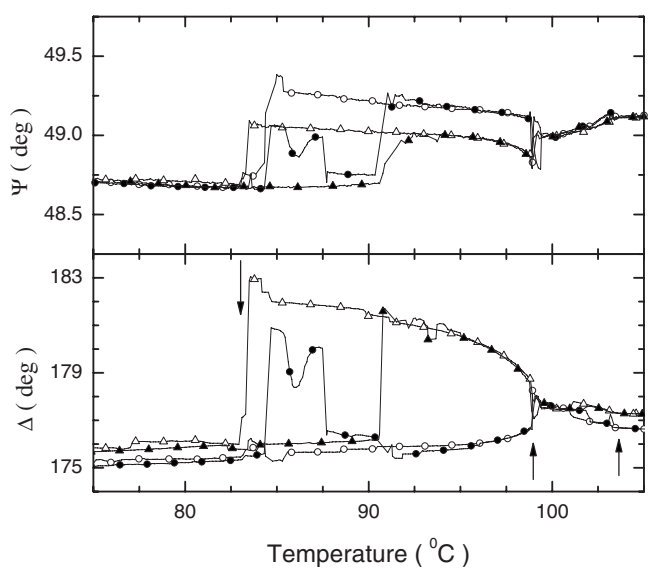

FIG. 10. Ψ and Δ vs temperature for an 85-layer film of 83% C11 with 17% 10OHF while ramping at 150 mK/min. The electric field orientation was held constant at α=90° (circles) or 270° (triangles) during each ramp. Both cooling (open symbols) and heating (filled symbols) are shown. Arrows mark the transition temperatures while cooling.

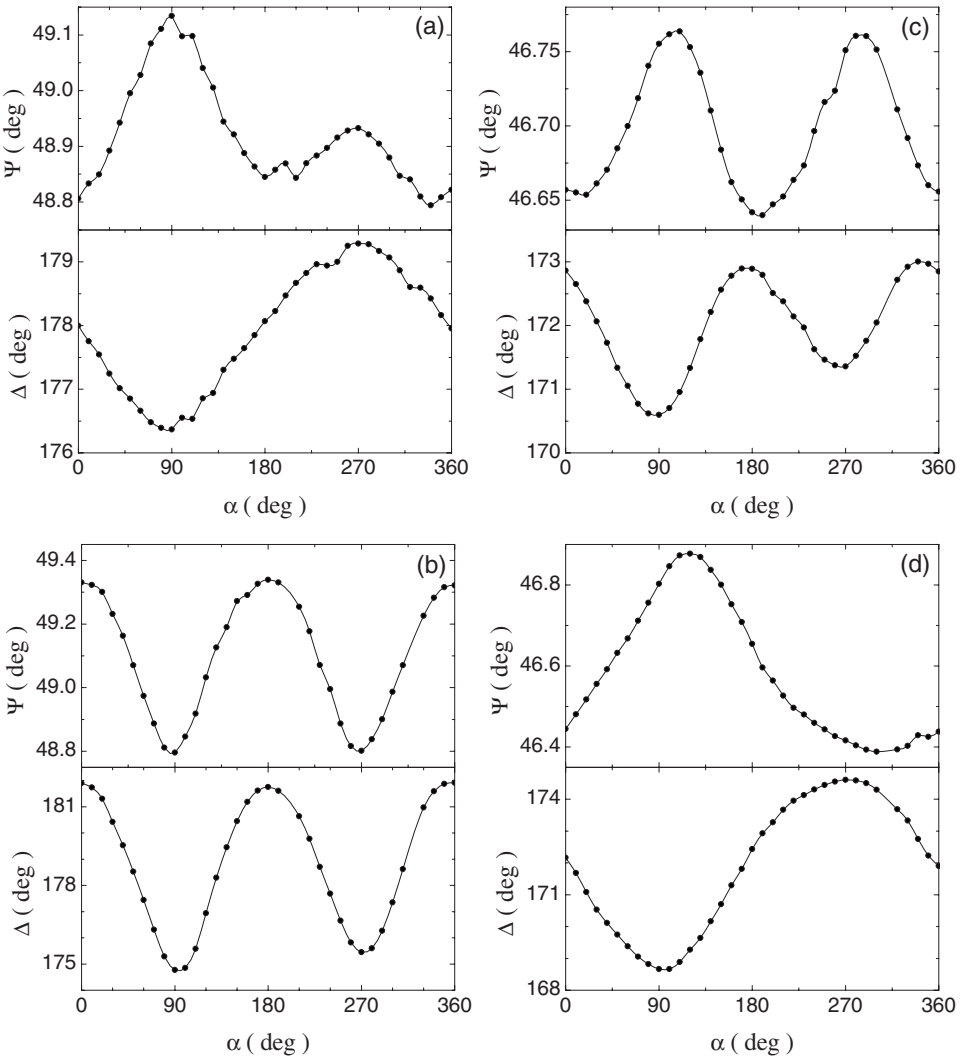

FIG. 11. Ψ and Δ vs α for (a) an 85-layer film of 83% C11 with 17% 10OHF at 97.7 and (b) 65.6 °C and (c) a 49-layer film of 11% C11 with 89% 10OHF at 72.6 and (d) 52.4 °C. The lines are guides to the eye.

K while heating. The SmC^*_{FI2} phase is thermotropic, just as in the mixtures of more than 10% C9 with 10OHF. In the mixture of 67% C11 (Fig. 9), SmC^* is not present at any temperature. There is a direct SmC^*_α-SmC^*_{FI2} transition at 87 °C. When the majority of the sample is C11, as in the mixture with 83% C11, the SmC^* phase occurs at higher temperature than SmC^*_{FI2} as in the normal phase sequence. In Fig. 10, the maximum temperature for the SmC^* phase is 99 °C. One transition appears at a higher temperature, 103 °C; however Δ did not oscillate between 99 and 103 °C even in thick films, as the SmC^*_α phase would. The transition at 103 °C is a surface transition between a synclinic arrangement of the two surfaces at high temperature to an anticlinic arrangement. Figure 10 also shows a hysteresis of about 8 K in the SmC^*-SmC^*_{FI2} transition.

The symmetries of the phases observed in the mixtures with 11% and 83% C11 with 10OHF are shown in Fig. 11. Only the phases at lower temperature than SmC^*_α are shown. Figures 11(a) and 11(d) show a single minimum in Δ near α=90°, characteristic of the SmC^* phase. In Figs. 11(b) and 11(c), two minima occur in both Ψ and Δ and the curves of Ψ and Δ have approximately 180° symmetry, indicating either the SmC^*_{FI2} or SmC^*_A phase [25]. Because the data in Figs. 11(a) and 11(c) were taken at higher temperatures than the data in Figs. 11(b) and 11(d), we can see that the phase sequence is inverted.

Figure 12 shows typical RXRD scans in each tilted smectic phase of the mixture of 11% C11 with 89% 10OHF. This mixture has the smallest percentage of a sulfur-containing dopant successfully studied using RXRD to date. The x-ray energy was tuned to E_o=2.475 keV, near the sulfur absorption edge. The size of the unit cell, calculated from the spacing between the (001) Bragg peak and the resonant peak, in Fig. 12(a) is 5.7 layers so the phase is SmC^*_α. The resonant peak in Fig. 12(b) is located at Q_z/Q_0=1.25 so the phase is SmC^*_{FI2}. The superposition of the l=1, m=1 and l=2, m=−2 resonant peaks produces a partially split peak due to the optical pitch of the SmC^*_{FI2} phase [26]. Fitting of the split peak yields an optical pitch of 588 layers and a distortion angle of 9°. The resonant peak in Fig. 12(c) sits on the shoulder of the (002) Bragg peak; the helical pitch is 135 layers and the phase is SmC^*. Another scan over the same range of Q_z with the x-ray energy detuned from the resonant energy E_0 shows only the tail of the Bragg peak, confirming that the peak in Fig. 12(c) is a resonant peak due to the azimuthal ordering of the SmC^* phase. The phase sequence is confirmed to be SmA-SmC^*_α-SmC^*_{FI2}-SmC^* for this mixture, the same phase sequence as for pure 10OHF upon cooling.

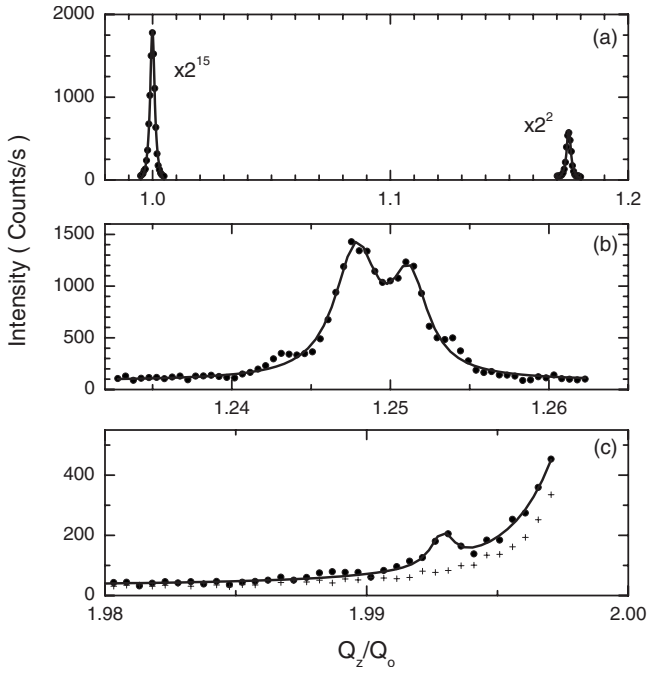

FIG. 12. Scans for 11% C11 with 89%10OHF at (a) 81.87, (b) 63.61, and (c) 58.50 °C. The solid lines are double Lorentzian fits. In (a) filter units attenuated the beam intensity by a factor of 2^{15} for the Bragg peak and a factor of 2^2 for the resonant peak. The crosses in (c) are data obtained with the x-ray energy increased by 10 eV from the resonant energy. At each temperature, the data are scaled so that the (001) Bragg peak appears at $Q_z/Q_0=1$ where $Q_0=2\pi/d$ and d is the layer spacing.

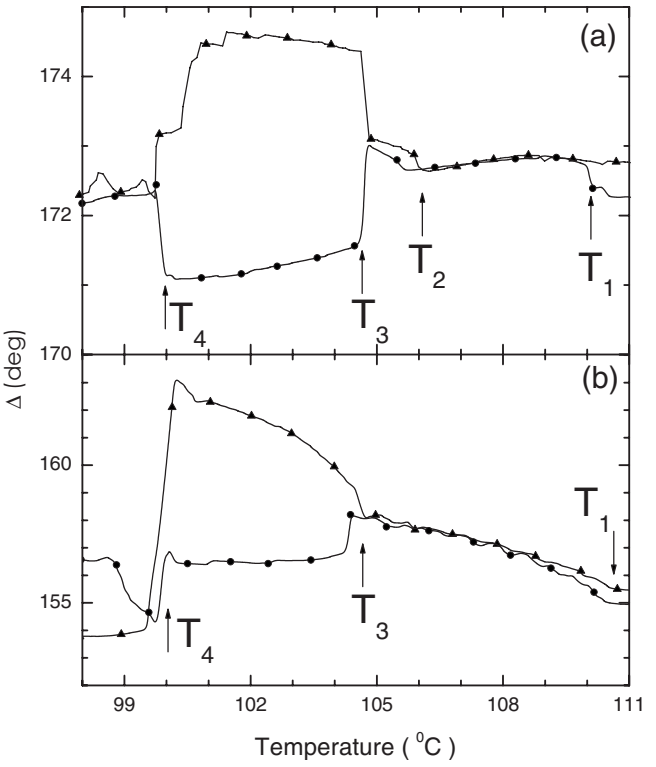

FIG. 13. Δ vs temperature for (a) a 43- and (b) a 395-layer film of 74.4% C11 with 25.6% 10OHF while ramping at 150 mK/min. The electric field orientation was held constant at $\alpha=90°$ (circles) or 270° (triangles) during each ramp. The arrows in (a) mark four transition temperatures.

VI. REENTRANT TRANSITION IN THIN FILMS

Figure 13 shows NTE data for 43- and 395-layer films as a function of temperature at two opposite orientations of the electric field for a mixture with 74.4% C11 and 25.6% 10OHF. This mixture was chosen to investigate the point where the SmC^* phase disappears from the mixing phase diagram for $x>50\%$. Another mixture with 72% C11 and 28% 10OHF showed similar behavior. Arrows mark four transition temperatures in Fig. 13. The transition temperatures depend on the film thickness. Above T_1 the phase is optically uniaxial SmA. The difference in Δ at the two orientations above T_1 in Fig. 13 is due to biaxial surface layers. The oscillations in Δ between T_1 and T_3 in Fig. 13(b) identify the SmC^*_α phase [27]. For the thinner film in Fig. 13(a), the number of turns of the $\vec{c}$ helix changes more slowly with temperature so only a partial oscillation occurs, as shown by the small hump in Δ between T_1 and T_2 [16]. Figure 14 contains data for a 17-layer film obtained while rotating α in 10° steps at three temperatures for which the sample was in one of the tilted smectic phases: $T_5=105.3$ °C, just above T_3 for this film thickness, $T_6=103.5$ °C, between T_3 and T_4, and $T_7=97.2$ °C, below T_4. Similar data sets were obtained from 21 films of different thicknesses; the data from the 17-layer film are shown here because of the decreased number of parameters necessary for the fitting, to be discussed later. From the relatively large change in Δ with α, we see that the film is biaxial in all of these subphases. At T_6, the film has no rotational symmetry around the film normal. The single prominent minimum in Δ at $\alpha=90°$ occurs because the $\vec{c}$ vectors are parallel for all interior layers and perpendicular to the net polarization; this is the SmC^* phase. The Δ and Ψ vs α curves at both T_5 and T_7 have approximately 180° symmetry, indicating an antiferroelectric phase, either SmC^*_{FI2} or SmC^*_A [25]. Moreover, the Ψ vs Δ curves at T_5 and T_7 have very similar shapes, suggesting that these are the same phase. The larger amplitude of Ψ and Δ vs temperature at T_7 is due to an increase in the tilt angle and the biaxiality as the temperature decreases.

We can obtain more details about the structure from simulations using the 4×4 matrix method [28]. The indices of refraction n_o and n_e and the layer spacing were determined by matching simulations in the SmA phase to data from films of 44 different thicknesses [10]. The SmC^* phase in Fig. 14 (crosses) is easiest to fit. The amplitude of the Ψ and Δ vs α curves determines the tilt angle $\theta_{\text{bulk}}=16.5°$. The simulation shown by the dashed lines in Fig. 14 uses parallel tilts in all of the layers. This model produces one minimum in Δ vs α, clearly not in agreement with the data. In order to produce the second minimum in Δ vs α at $\alpha=270°$, four antiferroelectric layers at each surface ($\theta_{\text{surf}}=17.5°$) are necessary. When two minima of Δ vs α are present, two loops in the Ψ vs Δ curves appear. The number of antiferroelectric surface layers is determined by the angle between the two loops of the Ψ vs Δ curve. The number of antiferroelectric surface layers is consistent with the observed biaxiality in the SmA

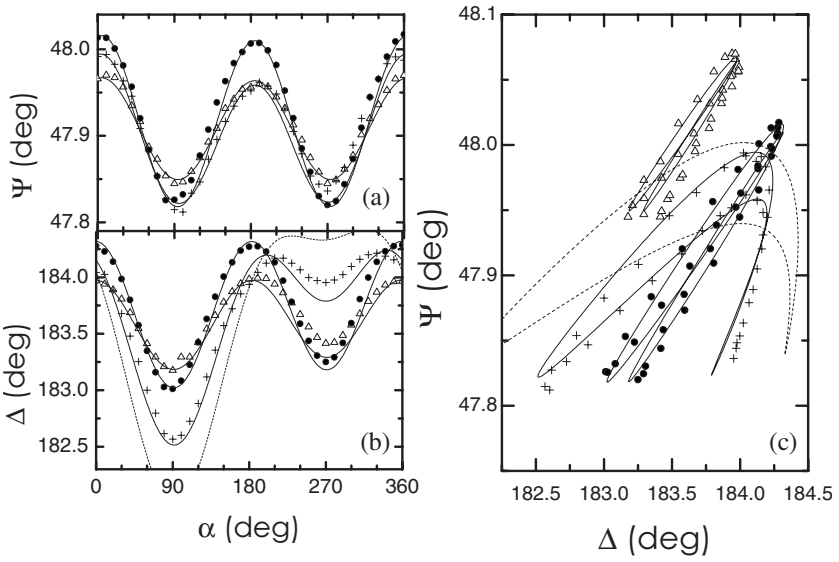

FIG. 14. (a) Ψ vs α, (b) Δ vs α, and (c) Ψ vs Δ obtained by NTE at $T_5=105.3$ °C (triangles), $T_6=103.5$ °C (crosses), and $T_7=97.2$ °C (solid circles). The solid lines are results of simulations using the 4×4 matrix method. The dashed lines are alternate simulations as described in the text. In (c), the data at T_5 are shifted upward in Ψ by 0.1° for clarity.

phase [15]. At T_7, the film is biaxial and antiferroelectric. A simulation with $\theta_{\text{bulk}}=\theta_{\text{surf}}=19.2°$ and antiparallel tilts in adjacent layers, the SmC_A^* structure, fits the data well; however, this structure will be ruled out later. The simulation shown uses four antiferroelectric layers per surface, consistent with the simulation in SmC^*, and an Ising-like SmC_{FI2}^* structure in the interior layers; this structure gives two loops of similar size in the Ψ vs Δ curve as occur in the data. The data at T_5 also show that the film is biaxial and antiferroelectric, either SmC_A^* or SmC_{FI2}^*. A SmC_A^* structure fits these data well. If SmC_A^* occurs at higher temperature than SmC^*, this would be a very surprising and important finding. Alternatively, an Ising-like SmC_{FI2}^* interior with antiferroelectric surface layers, just as at T_7, produces two loops in the Ψ vs Δ curve of nearly equal size, matching the data. The simulations for T_5 and T_7 in Fig. 14 use exactly the same structure except that at T_5 the tilt angles are $\theta_{\text{bulk}}=12°$ and $\theta_{\text{surf}}=17.5°$.

To gain still more confidence in the identity of the phases, we have also performed RXRD studies. Figure 15 shows scans of the resonant peaks at three representative temperatures for each tilted smectic subphase observed by NTE. In Fig. 15(a), the unit cell is 10.1 smectic layers; the phase is SmC_α^*. The resonant peak in Fig. 15(b) sits on the shoulder of the (002) Bragg peak, indicating a long helical pitch of 103 smectic layers. This confirms that the phase is SmC^*. The resonant peak position in Fig. 15(c) yields a four-layer unit cell. This rules out SmC_A^* as the structure observed at T_7 by NTE. The scan in Fig. 15(c) with the energy detuned from the $K\alpha$ edge of sulfur verifies that these are resonant peaks. We were not able to observe a phase between SmC_α^* and SmC^* with RXRD. While the NTE data alone cannot guarantee that the structure at T_5 is SmC_{FI2}^*, it is highly unlikely that the more ordered SmC_A^* phase would occur at a higher temperature than both SmC^* and SmC_{FI2}^*. Combined with the observation that the shapes of the Ψ vs Δ curves at T_5 and T_7 are similar, we can infer that the structure at T_5 is SmC_{FI2}^* and that the sample therefore exhibits a reentrant SmC_{FI2}^*-SmC^*-SmC_{FI2}^* transition in thin free-standing films.

The reentrant SmC_{FI2}^*-SmC^*-SmC_{FI2}^* transition was observed in several films with thicknesses up to 153 layers. However, for the 395-layer film in Fig. 13(a), there is a direct transition from SmC_α^* to SmC^* instead of SmC_{FI2}^* between SmC_α^* and SmC^* [29]. The temperature window for the SmC_{FI2}^* phase above the SmC^* phase decreased with increasing film thickness, as seen in Fig. 16. The large variations in T_2-T_3 are due to the first-order nature of the SmC_{FI2}^*-SmC^*

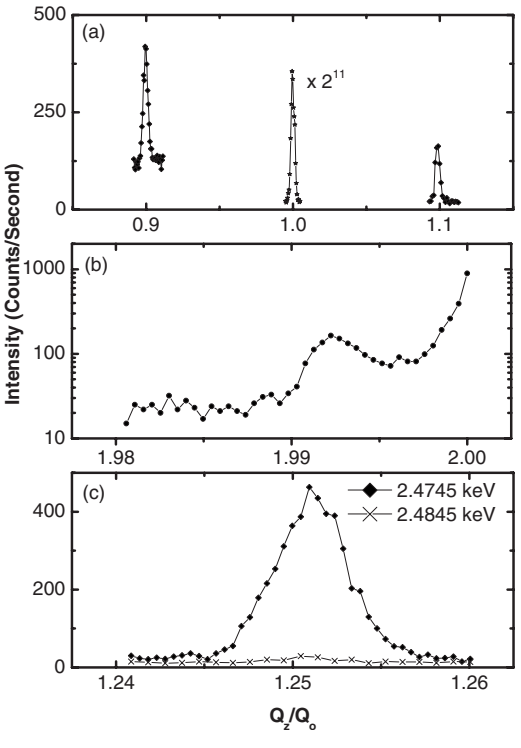

FIG. 15. (a) RXRD scans for 74.4% C11 and 25.6% 10OHF at 109.8 °C. Q_0 is the reciprocal lattice vector corresponding to the (001) reflection. The (001) peak intensity is scaled down by a factor of 2^{11} for comparison. (b) The resonant peak at 103.9 °C sits on the tail of the (002) peak, located just off scale to the right. (c) RXRD scan of the resonant peak at 89.7 °C. The data shown by diamonds are resonant peaks and the stars are the (001) peak. The data shown by crosses were obtained with the x-ray energy detuned away from the $K\alpha$ edge of sulfur by 10 eV.

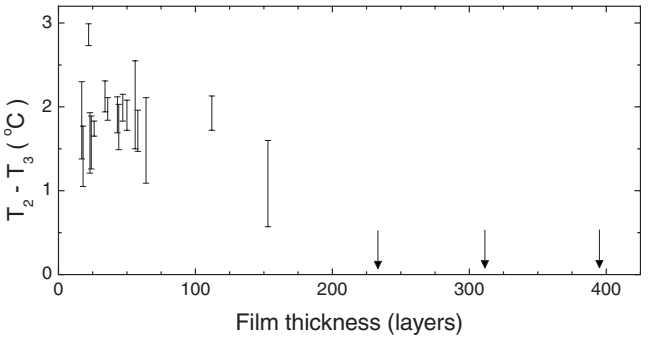

FIG. 16. Temperature range for the SmC^*_{FI2} phase above SmC^* for several film thicknesses. The transition temperatures were identified from Ψ and Δ vs temperature data during cooling ramps. The downward arrows represent thicknesses that were studied using NTE in which the reentrant transition did not occur.

transition. The reentrant transition occurs only in thin films [30]. This explains why we could not observe the reentrant transition using RXRD, because RXRD requires films several hundred layers thick to obtain a sufficient scattering signal. Surfaces in free-standing smectic films are known to interact over a long range [31], even though the mechanism for this interaction is not well understood [32]. The existence of an interaction is particularly apparent while the bulk of the film is in the Sm*A* phase; except in very rare cases [24,33], the tilted surface layers remain in Ising-like states even for thick films [34,35]. Such interactions between the surfaces may well persist even when the bulk of the film enters the tilted smectic subphases rather than Sm*A*. Qualitatively, interactions between the surfaces should depend on temperature and the thickness of the film. Surface interactions also will likely affect the nearby interior layers, potentially introducing an effective long-range interaction to the bulk. According to one recent theory [21,22], a long-range interaction stabilizes the SmC^*_{FI2} phase. The effective long-range interaction due to the surfaces may similarly stabilize the SmC^*_{FI2} phase, leading to the reentrant transition that we observe. The results of Fig. 16 suggest that the range of the surface interactions is fairly long.

VII. SUMMARY

We have used NTE and RXRD to identify the phase sequences for several mixtures of C9 or C11 with 10OHF. We have extended the result of Ref. [3] to show that the SmC^*_{FI2} phase is stabilized upon doping for both $x<50\%$ and $x>50\%$ in the phase diagram in Fig. 6. Figure 17 summarizes the phase diagram for binary mixture of C11 with 10OHF. The temperature window for SmC^*_{FI2} increases with increasing percentage of C11 until SmC^* is eliminated from the

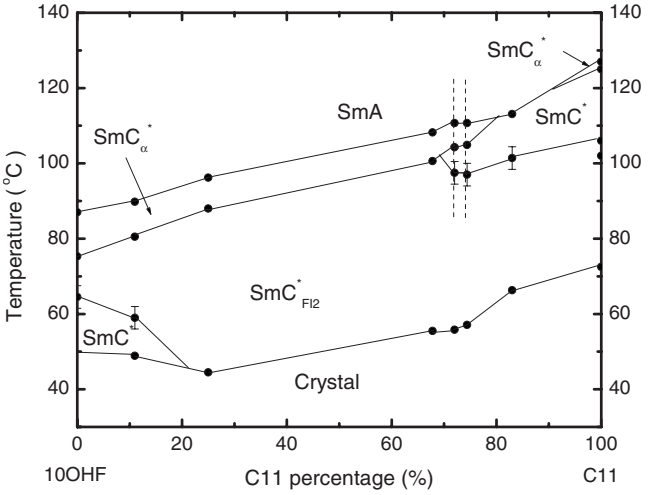

FIG. 17. Phase diagram for binary mixtures of 10OHF with C11. The circles mark the transition temperatures for each mixture studied. All data shown was obtained from films at least 60 layers thick. For the mixtures studied using RXRD, the film thickness was more than 500 layers. Error bars represent hysteresis in the transition temperatures. The dashed lines mark the two mixtures for which the reentrant SmC^*_{FI2}-SmC^*-SmC^*_{FI2} transition was observed.

phase sequence. The SmC^* phase is also squeezed out of the phase diagram on the C11-rich side. The SmC^*_{FI2} phase is stabilized by mixing. This supports the conclusion of Ref. [3] that the unusual phase sequence of 10OHF and the SmC^*_{FI2} phase are perhaps more stable than previously thought.

Near the point where the SmC^* phase disappears from the C11-rich side of the C11-10OHF phase diagram ($x>50\%$), the SmC^* and SmC^*_{FI2} phases must be nearly degenerate. In this case, interactions from the surfaces of a free-standing film can make significant contributions to the film's free energy. We have found that in films thinner than about 150 layers, surface interactions induce the SmC^*_{FI2} phase at temperatures just below the SmC^*_α phase, resulting in a reentrant SmC^*_{FI2}-SmC^*-SmC^*_{FI2} transition.

ACKNOWLEDGMENTS

We are grateful to P. Barois for lending us his x-ray oven for the RXRD studies. Research at NSLS, BNL was supported in part by the U.S. Department of Energy, Division of Materials Sciences and Division of Chemical Sciences, under Contract No. DE-AC02-98CH10886. The research was supported in part by the donors of the Petroleum Research Fund, administered by the American Chemistry Society and by the National Science Foundation, Solid State Chemistry Program under Grants No. DMR-0106122 and No. DMR-0605760. B.K.M. and Z.Q.L. acknowledge support from the University of Minnesota Graduate School.

[1] L. S. Hirst, S. J. Watson, H. F. Gleeson, P. Cluzeau, P. Barois, R. Pindak, J. Pitney, A. Cady, P. M. Johnson, C. C. Huang, A.-M. Levelut, G. Srajer, J. Pollmann, W. Caliebe, A. Seed, M. R. Herbert, J. W. Goodby, and M. Hird, Phys. Rev. E **65**, 041705 (2002).

[2] P. G. DeGennes and J. Prost, *The Physics of Liquid Crystals* (Clarendon Press, Oxford, 1993).

[3] S. T. Wang, Z. Q. Liu, B. K. McCoy, R. Pindak, W. Caliebe, H. T. Nguyen, and C. C. Huang, Phys. Rev. Lett. **96**, 097801 (2006).

[4] S. Jaradat, N. W. Roberts, Y. Wang, L. S. Hirst, and H. F. Gleeson, J. Math. Chem. **16**, 3753 (2006).

[5] D. A. Olson, X. F. Han, P. M. Johnson, A. Cady, and C. C. Huang, Liq. Cryst. **29**, 1521 (2002).

[6] P. Mach, R. Pindak, A.-M. Levelut, P. Barois, H. T. Nguyen, C. C. Huang, and L. Furenlid, Phys. Rev. Lett. **81**, 1015 (1998).

[7] A.-M. Levelut and B. Pansu, Phys. Rev. E **60**, 6803 (1999).

[8] V. Laux, N. Isaert, V. Faye, and H. T. Nguyen, Liq. Cryst. **27**, 81 (2000).

[9] D. Schlauf, Ch. Bahr, V. K. Dolganov, and J. W. Goodby, Eur. Phys. J. B **9**, 461 (1999).

[10] D. A. Olson, S. Pankratz, P. M. Johnson, A. Cady, H. T. Nguyen, and C. C. Huang, Phys. Rev. E **63**, 061711 (2001).

[11] S. Heinekamp, R. A. Pelcovits, E. Fontes, E. Y. Chen, R. Pindak, and R. B. Meyer, Phys. Rev. Lett. **52**, 1017 (1984).

[12] Ch. Bahr and D. Fliegner, Phys. Rev. Lett. **70**, 1842 (1993).

[13] S. T. Wang, Ph.D. Thesis, University of Minnesota, 2006.

[14] K. L. Sandhya, Yu. P. Panarin, U. Manna, J. K. Vij, and S. Kumar, Phys. Rev. Lett. **98**, 219801 (2007).

[15] A. Cady, D. A. Olson, X. F. Han, H. T. Nguyen, and C. C. Huang, Phys. Rev. E **65**, 030701(R) (2002).

[16] Similar oscillations occur in NTE. [D. Schlauf, Ch. Bahr, and H. T. Nguyen, Phys. Rev. E **60**, 6816 (1999)].

[17] For the dependence of the phase sequence on enantiomeric excess, see E. Gorecka, D. Pociecha, M. Čepič, B. Žekš, and R. Dabrowski, Phys. Rev. E **65**, 061703 (2002); A. Cady, Z. Q. Liu, X. F. Han, S. T. Wang, M. Veum, N. Janarthanan, C. S. Hsu, D. A. Olson, and C. C. Huang, *ibid.* **66**, 061704 (2002).

[18] L. S. Matkin, S. J. Watson, H. F. Gleeson, R. Pindak, J. Pitney, P. M. Johnson, C. C. Huang, P. Barois, A.-M. Levelut, G. Srajer, J. Pollmann, J. W. Goodby, and M. Hird, Phys. Rev. E **64**, 021705 (2001).

[19] In contrast to the data reported in [36], our NTE and RXRD data show the Sm*A*-SmC^*_α-SmC^*_{FI2}-SmC^*_A transition sequence upon cooling for pure C9.

[20] D. A. Olson, X. F. Han, A. Cady, and C. C. Huang, Phys. Rev. E **66**, 021702 (2002).

[21] M. B. Hamaneh and P. L. Taylor, Phys. Rev. Lett. **93**, 167801 (2004).

[22] M. B. Hamaneh and P. L. Taylor, Phys. Rev. E **72**, 021706 (2005).

[23] Z. Q. Liu, S. T. Wang, B. K. McCoy, A. Cady, R. Pindak, W. Caliebe, K. Takekoshi, K. Ema, H. T. Nguyen and C.C. Huang, Phys. Rev. E **74**, 030702(R) (2006).

[24] X. F. Han, D. A. Olson, A. Cady, J. W. Goodby, and C. C. Huang, Phys. Rev. E **65**, 010704(R) (2001).

[25] P. M. Johnson, D. A. Olson, S. Pankratz, T. Nguyen, J. Goodby, M. Hird, and C. C. Huang, Phys. Rev. Lett. **84**, 4870 (2000).

[26] A. Cady, J. A. Pitney, R. Pindak, L. S. Matkin, S. J. Watson, H. F. Gleeson, P. Cluzeau, P. Barois, A.-M. Levelut, W. Caliebe, J. W. Goodby, M. Hird, and C. C. Huang, Phys. Rev. E **64**, 050702(R) (2001).

[27] P. M. Johnson, S. Pankratz, P. Mach, H. T. Nguyen, and C. C. Huang, Phys. Rev. Lett. **83**, 4073 (1999).

[28] D. W. Berreman, J. Opt. Soc. Am. **62**, 502 (1972); H. Wohler, G. Haas, M. Fritsch, and D. A. Mlynski, J. Opt. Soc. Am. A **5**, 1554 (1988).

[29] A set of slower heating and cooling runs with a ramp rate of 30 mK/min also did not show any phase between SmC^*_α and SmC^* for the 395-layer film.

[30] D. Pociecha, E. Gorecka, M. Čepič, N. Vaupotič, B. Žekš, D. Kardas, and J. Mieczkowski, Phys. Rev. Lett. **86**, 3048 (2001).

[31] C. Y. Chao, C. R. Lo, P. J. Wu, Y. H. Liu, D. R. Link, J. E. Maclennan, N. A. Clark, M. Veum, C. C. Huang, and J. T. Ho, Phys. Rev. Lett. **86**, 4048 (2001).

[32] B. Rovšek, M. Čepič, and B. Žekš, Phys. Rev. E **66**, 051701 (2002).

[33] B. K. McCoy, Z. Q. Liu, S. T. Wang, V. P. Panov, J. K. Vij, J. W. Goodby, and C. C. Huang, Phys. Rev. E **73**, 041704 (2006).

[34] D. R. Link, G. Natale, N. A. Clark, J. E. Maclennan, M. Walsh, S. S. Keast, and M. E. Neubert, Phys. Rev. Lett. **82**, 2508 (1999).

[35] X. F. Han, S. T. Wang, A. Cady, M. D. Radcliffe, and C. C. Huang, Phys. Rev. Lett. **91**, 045501 (2003).

[36] H. T. Nguyen, J. C. Rouillon, P. Cluzeau, G. Sigaud, C. Destrade, and N. Isaert, Liq. Cryst. **17**, 571 (1994).